

Emergence and stability of spin-valley entangled quantum liquids in moiré heterostructures

Dominik Kiese, Finn Lasse Buessen[✉], Ciarán Hickey[✉], Simon Trebst[✉], and Michael M. Scherer

Institute for Theoretical Physics, University of Cologne, 50937 Cologne, Germany



(Received 26 July 2019; revised manuscript received 7 February 2020; accepted 12 February 2020; published 30 March 2020)

Twisting moiré heterostructures to the flatband regime allows for the formation of strongly correlated quantum states, since the dramatic reduction of the bandwidth can cause the residual electronic interactions to set the principal energy scale. An effective description for such correlated moiré heterostructures, derived in the strong-coupling limit at integer filling, generically leads to spin-valley Heisenberg models. Here we explore the emergence and stability of spin-liquid behavior in an $SU(2)^{\text{spin}} \otimes SU(2)^{\text{valley}}$ Heisenberg model upon inclusion of Hund's-induced and longer-ranged exchange couplings, employing a pseudofermion functional renormalization group approach. We consider two lattice geometries, triangular and honeycomb (relevant to different moiré heterostructures), and find, for both cases, an extended parameter regime surrounding the $SU(4)$ symmetric point where no long-range order occurs, indicating a stable realm of quantum spin-liquid behavior. For large Hund's coupling, we identify the adjacent magnetic orders, with both antiferromagnetic and ferromagnetic ground states emerging in the separate spin and valley degrees of freedom. For both lattice geometries the inclusion of longer-ranged exchange couplings is found to have both stabilizing and destabilizing effects on the spin-liquid regime depending on the sign of the additional couplings.

DOI: [10.1103/PhysRevResearch.2.013370](https://doi.org/10.1103/PhysRevResearch.2.013370)

I. INTRODUCTION

Spurred by the discovery of a plethora of insulating and superconducting states in twisted bilayer graphene (TBG) [1,2], a growing stream of experimental evidence points to the generic emergence of correlated electronic behavior in various moiré heterostructures [3–12]. The basic mechanism that gives rise to strongly enhanced correlation effects in these materials is the formation of long-wavelength moiré patterns with (almost) flat low-energy bands whose narrow bandwidth becomes comparable to the otherwise negligible energy scale of the electronic interactions [13–15]. Due to a high degree of control, e.g., in the regulation of the twist angle, tunable bandwidths, or fillings, and a low level of disorder, such systems are discussed as ideal platforms for detailed studies of quantum many-body states. Despite a vast amount of concomitant theoretical activity [16–41], the precise nature of the observed insulators and superconductors, however, remains to be explored and settled through the construction of faithful models and application of appropriate quantum *many-body* approaches.

Several model constructions for correlated moiré materials have been put forward in terms of effective tight-binding descriptions on the moiré superlattice, augmented by various interaction terms [38,39,41]. Whereas details of the models may differ, they feature a series of universal

traits: (1) an emergent hexagonal superlattice, (2) a multiorbital structure, and (3) extended Hubbard and Hund's interactions. More specifically, while TBG is preferably described using a honeycomb superlattice [38,39,41], related structures such as, e.g., twisted double-bilayer graphene (TDBG) or trilayer graphene/hexagonal boron nitride heterostructures (TLG/h-BN) are better captured by a triangular superlattice [6,41–44]. The orbital degrees of freedom are inherited from the valleys in the original bands, e.g., the two Dirac valleys in the Brillouin zone of graphene.

Beyond these universal traits it has been argued that band topology can play an important role in moiré heterostructures [35,41,45–48]. Faithfully incorporating a nontrivial band topology in an effective tight-binding model and simultaneously maintaining all symmetries, for example, for TBG, is a formidable task, which can lead to complex multiband models that refuse a reduction to the flat bands only [49–51]. However, at least in some flat-band moiré heterostructures, including TLG/h-BN, the quantum valley topological number can be tuned from being nontrivial to being trivial by applying a perpendicular electric field [35,41,43]. In that latter case, the universal traits (1)–(3) may be combined into a minimal two-orbital extended Hubbard model [16,17] serving as a paradigmatic starting point. Its kinetic term

$$H_t = -t \sum_{\langle ij \rangle} \sum_{\alpha=1}^4 (c_{i\alpha}^\dagger c_{j\alpha} + \text{H.c.}), \quad (1)$$

for the electrons combines the spin projection $s \in \{\uparrow, \downarrow\}$ and valley quantum number $l \in \{+, -\}$ in a flavor index $\alpha \in \{(\uparrow, +), (\uparrow, -), (\downarrow, +), (\downarrow, -)\}$, reflecting an effective $SU(4)$ symmetry. On the triangular lattice this results in a set of four degenerate bands, which can potentially describe, e.g., the set

Published by the American Physical Society under the terms of the Creative Commons Attribution 4.0 International license. Further distribution of this work must maintain attribution to the author(s) and the published article's title, journal citation, and DOI.

of minibands above charge neutrality in TDBG or TLG/h-BN at appropriately tuned out-of-plane electric field.

The simplest conceivable interaction term retaining the SU(4) symmetry is a Hubbard interaction $H_{\text{int}} = U \sum_i (\sum_{\alpha=1}^4 n_{i\alpha})^2$, which can arise in the limit of large lattice periods where the interaction depends primarily on the total charge on a site and becomes the dominant interaction scale. In this strong-coupling limit, the kinetic term can then be treated perturbatively [16,17,41,43]. With an integer number of electrons per site this leads to an effective spin-valley Heisenberg Hamiltonian with SU(4) symmetric superexchange coupling $J_H \propto t^2/U$. Additional symmetry-breaking interactions are also expected, in particular in the form of further Hund's-type couplings in either the spin or valley degrees of freedom [16,17]. Moreover, Wannier state constructions suggest that further-neighbor interactions can become sizable [38] and should augment any minimal model. We note that for TLG/h-BN an intersite Hund's interaction has been argued to provide a leading ferromagnetic contribution to the nearest-neighbor exchange coupling in the strong-coupling limit [43]. Away from the strict limit, however, antiferromagnetic superexchange may dominate [43]. In this regime, the triangular geometry together with the additional valley degrees of freedom augments the role of quantum fluctuations suggesting that the system may host exotic quantum liquid behavior. In view of the large and ever-growing number of different correlated moiré heterostructures and the persistent interest in exotic quantum liquid behavior, we take this observation as a motivation to study generic antiferromagnetic spin-valley Heisenberg models. Further possible applications of such models are, e.g., Mott insulators with strong spin-orbit coupling [52–54].

More specifically, in this work, we explore antiferromagnetic nearest-neighbor spin-valley Heisenberg models with $SU(2)^{\text{spin}} \otimes SU(2)^{\text{valley}}$ symmetry for both triangular and honeycomb lattice geometries, which we later supplement with further-neighbor interaction terms. Our focus is on the case of half-filling of the underlying Hubbard model, i.e., two electrons per site. For the effective Heisenberg model at strong coupling, this implies that we are working with the six-dimensional self-conjugate representation of SU(4) spins. This is in contrast to the four-dimensional fundamental representation of SU(4) relevant to, e.g., the case of quarter-filling.

For both lattice geometries, we find extended parameter regimes surrounding the SU(4) symmetric point where no long-range symmetry-breaking order occurs, indicating a stable realm for a spin-valley entangled quantum liquid. Moving further away from the SU(4) symmetric point, we find magnetic order in the spin and valley degrees of freedom that can be either antiferromagnetic or ferromagnetic. To explore the effect of longer-range interactions, we augment our model by a next-nearest neighbor coupling and determine its role in stabilizing quantum spin-valley liquid (QSVL) behavior versus long-range order for different signs of the coupling and the two lattice geometries. Our work complements earlier work for the case of quarter-filling, where it was argued that a QSVL state with neutral gapless fermionic excitations forms on the honeycomb lattice [53], while on the triangular lattice extended parameter regimes without any net magnetization have been identified in DMRG simulations [55].

II. SPIN-VALLEY MODEL

The starting point of our study is an SU(4) spin-valley Heisenberg model [16,41], $\mathcal{H}_{\text{SU}(4)} = J_H \sum_{\langle ij \rangle} \hat{T}_i^\mu \hat{T}_j^\mu$, where J_H is the antiferromagnetic exchange coupling between nearest neighbors on either the triangular or honeycomb lattice, and \hat{T}_i denote SU(4) spins. The $\mu = 1, \dots, 15$ components of the spin operators can be represented on a fermionic Hilbert space via the parton construction $\hat{T}_i^\mu = f_{i\alpha}^\dagger T_{\alpha\beta}^\mu f_{i\beta}$, where the index α enumerates four different fermion flavors and the matrices T^μ are the SU(4) generators [56]. At half-filling of the underlying Hubbard model, the local spin-valley Hilbert space is six-dimensional (4 choose 2), which leads to a local filling constraint of two partons per lattice site $\sum_\alpha f_{i\alpha}^\dagger f_{i\alpha} = 2$.

Upon inclusion of Hund's couplings, the SU(4) symmetry of the model is explicitly broken [16]. Omitting other sources of SU(4) breaking, a residual separate spin-valley $SU(2)^s \otimes SU(2)^v$ symmetry remains which is reflected by the extended Hamiltonian

$$\mathcal{H} = \sum_{\langle ij \rangle} J (\hat{\sigma}_i^a \otimes \hat{\tau}_i^b) (\hat{\sigma}_j^a \otimes \hat{\tau}_j^b) + J_s \hat{\sigma}_i^a \hat{\sigma}_j^a + J_v \hat{\tau}_i^b \hat{\tau}_j^b, \quad (2)$$

where the spin-valley operators read $\hat{\sigma}_i^a = f_{is'l'}^\dagger \theta_{s's}^a \delta_{l'l} f_{isl}$, $\hat{\tau}_i^b = f_{is'l'}^\dagger \delta_{s's} \theta_{l'l}^b f_{isl}$, and $\hat{\sigma}_i^a \otimes \hat{\tau}_i^b = f_{is'l'}^\dagger \theta_{s's}^a \theta_{l'l}^b f_{isl}$. Instead of enumerating the four fermion types by a single index, we have exposed the spin quantum number $s \in \{\uparrow, \downarrow\}$ and the valley quantum number $l \in \{+, -\}$ explicitly; Pauli matrices are denoted by θ^a , $a \in \{1, 2, 3\}$. At the high-symmetry point $J = J_s = J_v$ the full SU(4) symmetry is restored. We assume that the Hund's interactions are weak enough such that all exchange couplings are antiferromagnetic [55], i.e., $J, J_v, J_s > 0$.

III. PSEUDOFOREMION FUNCTIONAL RG

Parton-decomposed quartic Hamiltonians of the general type defined in Eq. (2) can readily be analyzed by the pseudofermion functional renormalization group (pf-FRG) [57–60]. For $SU(N)$ spins, the approach is already naturally formulated with a local constraint of $N/2$ fermions per site. It combines aspects of an expansion in spin length S [61] (which naturally favors magnetic order) and in the $SU(N)$ spin symmetry [62,63] (which typically favors quantum spin-liquid states), and it becomes exact on a mean-field level in the separate limits of large S and large N . It is thus suited to resolve the competition between ordered ground states and QSVL phases in the spin-valley model at hand. We extend the standard implementation of pf-FRG to incorporate the $SU(2)^s \otimes SU(2)^v$ symmetry, thereby obtaining flow equations for the one-particle irreducible vertices as a function of an RG frequency cutoff scale Λ . Numerically solving the set of $\mathcal{O}(10^6)$ flow equations at up to 84 Matsubara frequencies and using a real-space vertex truncation of $L=7$ lattice bonds in each spatial direction, spontaneous symmetry breaking, e.g., the onset of long-range magnetic or valence bond order, is indicated by an instability of the RG flow [57,64] which occurs at some critical scale Λ_c .

In the case of long-range order, to identify the precise nature of the ordered state we can separately gain access to the elastic component ($\omega = 0$) of the correlation functions in

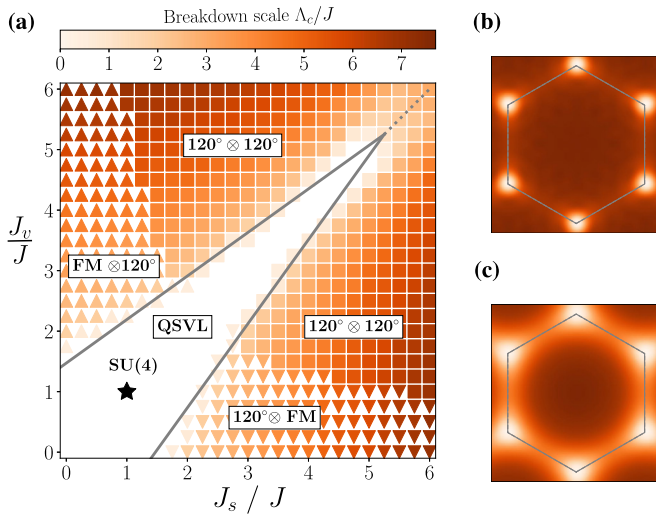


FIG. 1. Phase diagram on the triangular lattice. (a) Colors indicate the magnitude of the breakdown scale Λ_c in units of J , triangles (squares) denote regions with negative (positive) effective coupling Eq. (4); see text for details. (b) Structure factor in the spin (valley) subspace at dominant J_s (J_v), plotted at Λ_c , indicating the onset of 120° order. (c) Structure factor at the SU(4) point where no instability of the RG flow occurs. Local correlations are reminiscent of 120° order albeit broadened. The same color scale is applied to both (b) and (c). The solid gray lines mark the phase boundaries between the QSVL and the ordered phases, the dotted line marks the diagonal $J_s/J = J_v/J$.

the spin sector and in the valley sector,

$$\chi_{ij}^{s\Lambda} = \langle \hat{\sigma}_i^a \hat{\sigma}_j^a \rangle^\Lambda, \quad \text{and/or} \quad \chi_{ij}^{v\Lambda} = \langle \hat{\tau}_i^b \hat{\tau}_j^b \rangle^\Lambda. \quad (3)$$

Sharp features emerging in the respective structure factors $\chi^{s/v}(\vec{q}) \propto \sum_{ij} e^{i\vec{q} \cdot (\vec{r}_i - \vec{r}_j)} \chi_{ij}^{s/v}$ allow us to deduce the type of long-range order in either the spin or the valley degrees of freedom, cf. Figs. 1 and 2.

IV. EMERGENT SPIN-VALLEY LIQUID BEHAVIOR

We begin our analysis with the SU(4) symmetric point, $J_s/J = J_v/J = 1$. For both the triangular and honeycomb lattice, no instabilities are detected in the pf-FRG flow, indicating a fully symmetric ground state. In addition, upon varying the vertex range L we observe no finite-size dependence of the flows, consistent with a ground state without symmetry-breaking long-range order. This rules out not just magnetically ordered states, but also valence bond or dimer crystals [65], an ordering which spins in the self-conjugate representation are often prone to [66,67]. For SU(4) spins in the self-conjugate representation we can further use the Lieb-Schultz-Mattis-Hastings [68–70] theorem to rule out a featureless Mott insulator as the ground state in the case of the triangular lattice, whereas such a state is in principle still a possibility on the honeycomb lattice. We note that the spin/valley structure factors have features resembling 120° /Néel order, albeit significantly broadened; see Figs. 1(c) and 2(c).

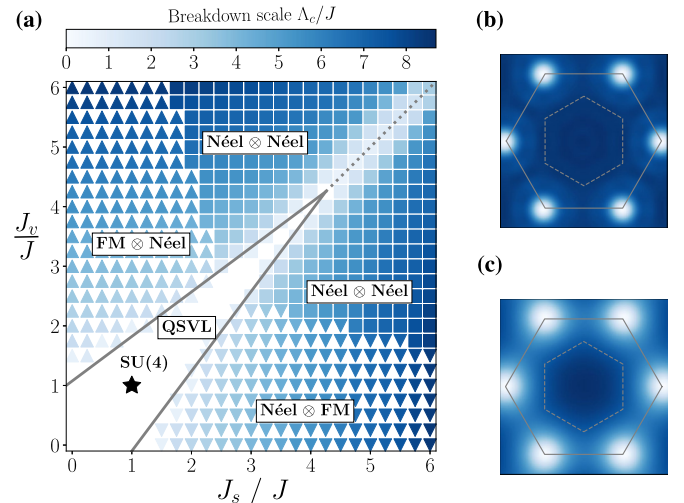


FIG. 2. Phase diagram on the honeycomb lattice. (a) Colors indicate the magnitude of the breakdown scale Λ_c in units of J , triangles (squares) denote regions with negative (positive) effective coupling Eq. (4); see text for details. (b), (c) Structure factors for a state deep in the Néel ordered phase versus the SU(4) symmetric state, with the same color scale applied.

V. STABILITY OF SPIN-VALLEY LIQUID AND ADJACENT MAGNETISM

Moving towards parameter regimes with broken SU(4) symmetry, $J_s/J, J_v/J \neq 1$, we find that an extended paramagnetic region emanates from the SU(4) symmetric point, see the white wedges in Figs. 1 and 2. Importantly, this finding supports the stability of the emergent spin-valley liquid behavior even in the presence of SU(4) breaking perturbations such as the Hund's coupling. Comparing the two lattice geometries, the triangular lattice gives rise to a parametrically larger QSVL phase than the bipartite honeycomb lattice, which can likely be traced back to the geometric frustration of the former. Along the diagonal line of equal coupling $J_v = J_s$, the QSVL region eventually collapses and disappears, being replaced by long-range antiferromagnetic order. Moving along the dotted diagonal line in the respective phase diagrams we observe a strongly suppressed breakdown scale Λ_c , relative to the surrounding parameter space, indicating that quantum fluctuations are strongest when $J_v = J_s$.

For sufficiently strong dominance of either spin or valley coupling, different ordered phases occur for both lattice geometries. The transition towards an ordered state is indicated by a leading instability in the RG flow, either in the spin or valley sector. To explore the subleading instabilities in the remaining sector, we employ a heuristic mean-field-like approach to estimate the effective spin or valley couplings between nearest-neighbor sites i and j ,

$$J_v^{\text{eff}} = J_v + J \chi_{ij}^{s\Lambda_c} \quad \text{and} \quad J_s^{\text{eff}} = J_s + J \chi_{ij}^{v\Lambda_c}. \quad (4)$$

Note that for 120° or Néel order in one of the SU(2) sectors the corresponding nearest-neighbor correlation becomes negative. Therefore, the effective couplings J_v^{eff} and J_s^{eff} may, too, turn negative and drive a *ferromagnetic* instability in the other sector, despite the antiferromagnetic nature of all couplings in

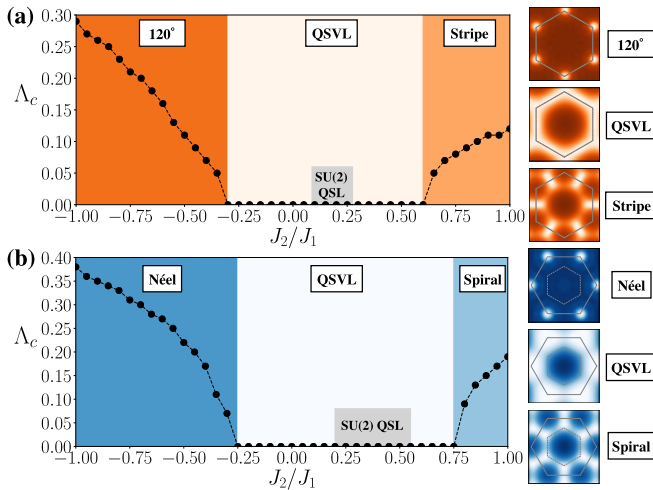


FIG. 3. Phase diagrams for $SU(4)$ J_1 - J_2 models on the triangular lattice (a) and the honeycomb lattice (b). Gray boxes indicate the extent of the quantum spin-liquid (QSL) regime for the respective spin-1/2 $SU(2)$ model. Structure factors for the respective phases are shown to the right, where the same color scale is applied to all plots of the underlying lattice.

the microscopic spin-valley model [55]. This kind of mechanism may be at the origin of the spin polarization observed at half-filling in TDBG [9,10], as first pointed out in Ref. [55] for quarter-filling. Extracting the sign of the effective coupling according to Eq. (4) at the transition scale of the leading sector allows us to distinguish two regimes with either ferro- or antiferromagnetic correlations in the subleading sector [71]. In Figs. 1 and 2 the so-determined order in the subleading regimes is indicated by triangle (ferromagnetic) or square (antiferromagnetic) symbols.

VI. LONGER-RANGE INTERACTIONS

In the ongoing search for an effective microscopic description for moiré heterostructures it has been pointed out that longer-ranged Coulomb interactions should not be neglected [38], which in the effective spin model will give rise to exchange couplings beyond nearest-neighbor. To probe the stability of the QSVL regime in our model we here consider the effect of a next-nearest neighbor coupling J_2 .

Let us first recapitulate the effect a next-nearest-neighbor coupling J_2 for the spin-1/2 $SU(2)$ case on the triangular and the honeycomb lattices. Here the bare nearest-neighbor coupling leads to magnetic ordering and only an antiferromagnetic J_2 of intermediate coupling strength facilitates the formation of a narrow quantum spin-liquid (QSL) regime [59,72–74], as indicated by the gray boxes in Fig. 3. Notably, the induced QSL regime is somewhat larger for the honeycomb lattice where the next-nearest neighbor interaction introduces geometric frustration.

For the model at hand, we first concentrate on the $SU(4)$ symmetric point and explore the effect of $J_2/J_1 \in [-1, 1]$. As shown in Fig. 3, the QSVL region for the $SU(4)$ model is significantly expanded for both lattice geometries in comparison to the $SU(2)$ QSL case. The impact of J_2 on the the full spin-valley (J_s, J_v) phase diagrams of Figs. 1 and 2 is

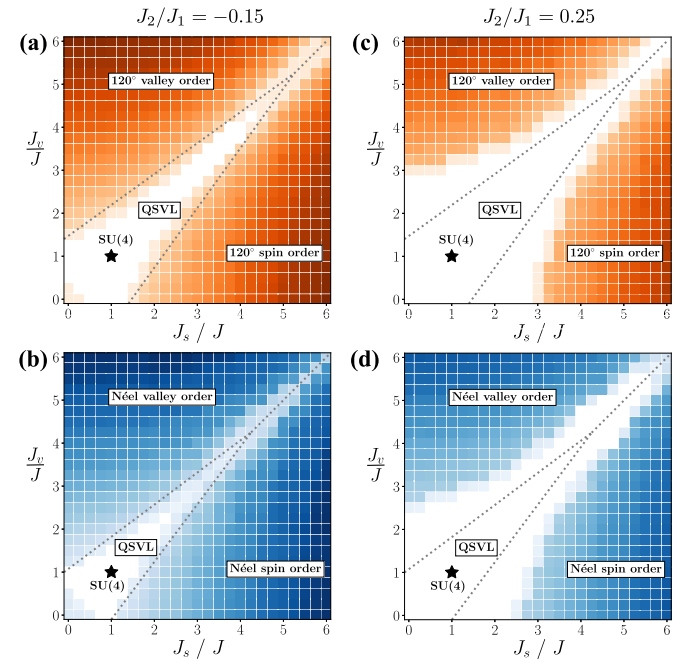


FIG. 4. Phase diagrams for longer-ranged spin-valley model showing the effect of ferromagnetic $J_2/J_1 = -0.15$ for (a) the triangular and (b) the honeycomb model. The same for antiferromagnetic $J_2/J_1 = 0.25$ for (c) the triangular and (d) the honeycomb model. Colors correspond to critical scales as indicated in Figs. 1 and 2. For reference, the phase boundaries at $J_2/J_1 = 0$ and the diagonal are marked by dotted lines.

illustrated in Fig. 4 for both ferromagnetic and antiferromagnetic J_2 . While an antiferromagnetic J_2 is found to further widen the wedge-shaped QSVL region, the converse occurs for ferromagnetic J_2 , which drives the system closer to the ordered states. This means that, depending on the sign of J_2 , longer-range interactions can actually stabilize and even expand the region of QSVL behavior.

VII. CONCLUSIONS

In this work, we studied $SU(2)^S \otimes SU(2)^V$ -symmetric spin-valley Heisenberg models in the self-conjugate representation for both the triangular and honeycomb lattice. Seen as the effective Hamiltonians generated in the strong-coupling limit of an underlying Hubbard model, such models are relevant as minimal models in the exploration of the correlated insulating states of recently synthesized moiré heterostructures. Depending on which set of minibands the Hubbard model is designed to describe, the half-filling case studied here can potentially describe different candidate correlated insulators, e.g., the insulator at half-filling $n = +n_s/2$ in the triangular system TDBG.

In particular, we focused on the study of Hund's-induced as well as longer-ranged exchange couplings and their impact on the spin-valley liquid which has been found to emerge in the limit of $SU(4)$ symmetry in both lattice geometries. We find extended parameter regimes where this phase is stabilized, with no signatures of long-range order, providing evidence for a stable realm of spin-valley liquid behavior. Experimentally,

such a phase would be consistent with a correlated insulator lacking spin and valley polarization. However, the precise nature of the phase and potential experimental fingerprints are left for future study, though we note that a recent projective-symmetry-group classification of fermionic partons on the half-filled triangular lattice suggests the possibility of a U(1) spin liquid with four Fermi surfaces [75], which would be consistent with our analysis. Our findings hint at the possibility of spin-valley entangled quantum liquids lurking within the correlated insulating regimes of moiré heterostructures.

ACKNOWLEDGMENTS

We thank L. Classen, P. Corboz, A. Laeuchli, and A. Paramekanti for discussions. C.H. thanks the Aspen Center for Theoretical Physics, where parts of this paper were written, for hospitality and support under Grant No. NSF 1066293. We acknowledge partial support from the Deutsche Forschungsgemeinschaft (DFG, German Research Foundation), Project No. 277146847, SFB 1238 (Project No. C03) and Project No. 277101999, TRR 183 (Projects No. B01 and No. A02). The numerical simulations were performed on the CHEOPS cluster at RRZK Cologne and the JURECA Booster at the Forschungszentrum Juelich.

APPENDIX A: HEXAGONAL MOIRÉ STRUCTURES

As noted in the main text, the minimal model that covers the necessary universal aspects of the various moiré heterostructures is a two-orbital extended Hubbard model. With four flavors of fermions per site, two spin and two valley degrees of freedom, this leads to a four band model on the triangular lattice and an eight band model on the honeycomb lattice (where the doubling is simply due to the doubling of the unit cell). Which of these lattices is appropriate to use depends on the particular moiré heterostructure one is interested in.

For TBG, TLG/h-BN, and TDBG there are a total of eight minibands near charge neutrality, four above and four below, that are separated from the rest of the spectrum by trivial band gaps. Filling of these minibands is thus typically denoted as ranging from $n = -n_s$ to $n = +n_s$, as indicated in Fig. 5 [where, for convenience, we plot $n/(n_s/4)$]. In the case of TBG, the bands above/below charge neutrality are connected

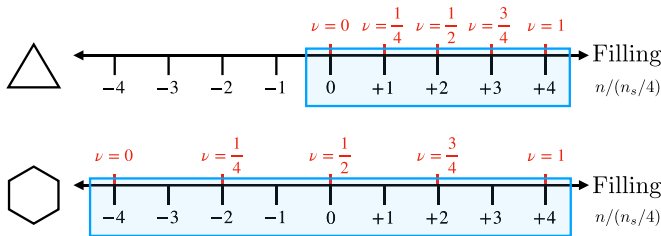


FIG. 5. Comparison of filling for the effective Hubbard model, ν , and for the minibands in the experimental cases of interest, $n/(n_s/4)$ (where $n = \pm n_s$ corresponds to fully empty or filled bands) in the case of a triangular (upper) and honeycomb (lower) lattice description. Depending on the lattice description the effective Hubbard model can either apply to all of, or just half of, the minibands, with its region of applicability denoted by the blue boxes.

via Dirac points, meaning that any effective Hubbard model must describe all eight bands. This naturally motivates the use of the honeycomb lattice Hubbard model. Half-filling, i.e., the scenario focused on in the main text, thus corresponds to charge neutrality $n = 0$. However, in the case of TDBG and TLG/h-BN the bands above/below charge neutrality are disconnected from one another, meaning that an effective Hubbard model description need only focus on one or the other set of four bands. This naturally leads to a triangular lattice description, with half-filling now corresponding to $n = \pm n_s/2$.

APPENDIX B: PSEUDOFERMION FUNCTIONAL RG APPROACH

The pseudofermion functional renormalization group (pf-FRG) has recently been established as a versatile tool for the investigation of ground state phase diagrams for a wide class of spin models [57, 76, 77]. In doing so, the free fermion propagator $G_0 = (i\omega)^{-1}$ of a pseudofermion decomposed quartic Hamiltonian, e.g., Eq. (1) (main text), is modified by a step-like regularization function $\Theta(|\omega| - \Lambda)$ with frequency cutoff scale Λ , i.e., $G_0 \rightarrow G_0^\Lambda = G_0 \Theta^\Lambda$. The artificial scale dependence of this theory results in a hierarchy of coupled one-loop RG flow equations for the one-particle-irreducible (1PI) interaction vertices. We employ a standard approximation scheme, where the hierarchy is truncated to exclusively account for the frequency-dependent self-energy Σ^Λ and two-particle interaction vertex Γ^Λ ; see, e.g., Ref. [62] for more details and technicalities.

Here, we describe the aspects of the pf-FRG which are particular to the present spin-valley model, i.e., the vertex parametrization for the $SU(2) \otimes SU(2)$ symmetry and the implementation of the filling constraint.

1. Vertex parametrization for $SU(2) \otimes SU(2)$ symmetry

The flow equations for the special case of $SU(2)^S \otimes SU(2)^V$ symmetry can be extracted from the general fermionic FRG equations. Here we consider the flows of the self-energy and the two-particle vertex given by

$$\frac{d}{d\Lambda} \Sigma^\Lambda(1'; 1) = -\frac{1}{2\pi} \sum_2 \Gamma^\Lambda(1', 2; 1, 2) S^\Lambda(2), \quad (B1)$$

$$\begin{aligned} \frac{d}{d\Lambda} \Gamma^\Lambda(1', 2'; 1, 2) &= -\frac{1}{2\pi} \sum_{3,4} [\Gamma^\Lambda(1', 2'; 3, 4) \Gamma^\Lambda(3, 4; 1, 2) \\ &\quad - \Gamma^\Lambda(1', 4; 1, 3) \Gamma^\Lambda(3, 2'; 4, 2) - (3 \leftrightarrow 4) \\ &\quad + \Gamma^\Lambda(2', 4; 1, 3) \Gamma^\Lambda(3, 1'; 4, 2) + (3 \leftrightarrow 4)] \\ &\quad \times G^\Lambda(3) \frac{d}{d\Lambda} G^\Lambda(4), \end{aligned} \quad (B2)$$

where the numbers $n = \{i_n, s_n, l_n, w_n\}$ represent tuples, comprising a lattice site index i_n , a spin index s_n , a valley index l_n and a Matsubara frequency w_n . We already employed that both the full G^Λ and single-scale S^Λ propagator are diagonal

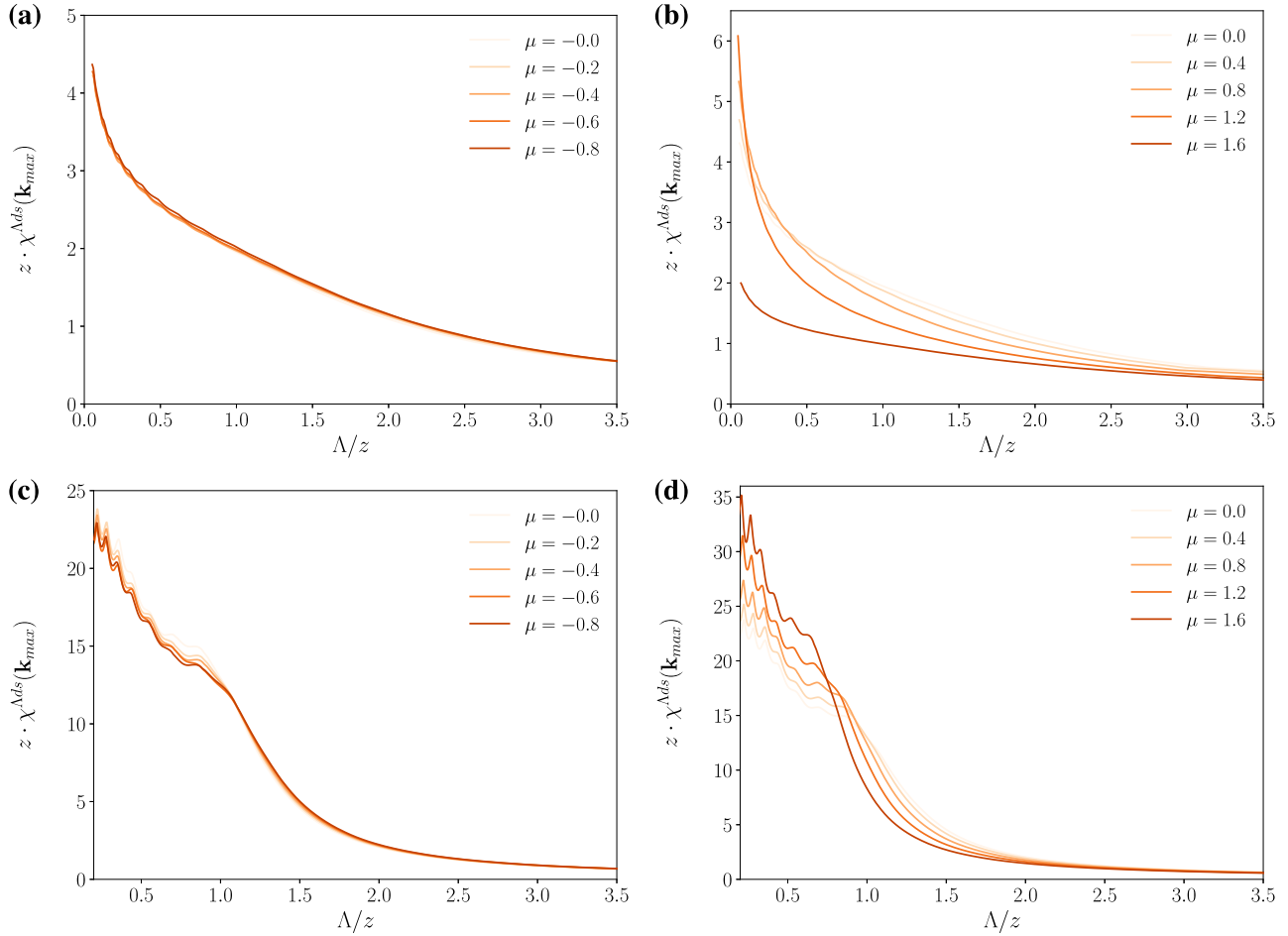


FIG. 6. Effect of level terms on the static structure factor $\chi^{\Lambda ds}(\mathbf{k})$ for the triangular lattice. (a), (b) $J_s/J = J_v/J = 1.0$. (c), (d) $J_s/J = 0.5, J_v/J = 4.0$. Negative μ yield no qualitative changes at $\mathbf{k} = \mathbf{k}_{\max}$ where the structure factor exhibits its peak value. For $\mu > 0$, especially in the QSVL phase, the flows differ visibly. Note that all axis have been normalized to a common energy scale by $z = \sqrt{J^2 + J_s^2 + J_v^2 + \mu^2}$ to account for the change of initial conditions.

in all arguments. Their remaining frequency dependence is given by

$$G_i^\Lambda(w) = \frac{\theta(|\omega| - \Lambda)}{iw - \Sigma_i^\Lambda(w)}, \quad (\text{B3})$$

$$S_i^\Lambda(w) = \frac{\delta(|\omega| - \Lambda)}{iw - \Sigma_i^\Lambda(w)}. \quad (\text{B4})$$

The spin/valley dependence of the 1PI irreducible vertices can then be expanded in terms of an $\mathfrak{su}(2)$ basis. Augmenting this scheme by symmetry-allowed SU(2)-invariant density terms and making use of translation invariance in imaginary time, as well as local $U(1)$ symmetry, the parametrization of the vertices reads

$$\Sigma^\Lambda(1'; 1) = \sum_{\alpha, \beta} \Sigma_{i_1}^{\Lambda\alpha\beta}(w_1) \theta_{s_1, s_1}^\alpha \theta_{l_1, l_1}^\beta \delta_{i_1, i_1} \delta(w_{1'} - w_1), \quad (\text{B5})$$

$$\begin{aligned} \Gamma^\Lambda(1', 2'; 1, 2) &= \sum_{\alpha, \alpha', \beta, \beta'} \Gamma_{i_1 i_2}^{\Lambda\alpha\alpha'\beta\beta'}(w_1, w_2; w_1, w_2) \theta_{s_1, s_1}^\alpha \theta_{s_2, s_2}^{\alpha'} \theta_{l_1, l_1}^\beta \theta_{l_2, l_2}^{\beta'} \delta_{i_1, i_1} \delta_{i_2, i_2} \\ &\times \delta(w_{1'} + w_{2'} - w_1 - w_2) - (1 \leftrightarrow 2), \end{aligned} \quad (\text{B6})$$

where $\alpha, \beta \in \{0, 1, 2, 3\}$ with $\theta^0 = \mathbf{1}$. Exploiting SU(2) symmetry in both spin and valley indices we are left with pure density contributions for the self-energy, while the two-particle vertex may also contain off-diagonal terms albeit with equal spin directions, i.e.,

$$\Sigma^\Lambda(1'; 1) = \Sigma_{i_1}^\Lambda(w_1) \delta_{s_1, s_1} \delta_{l_1, l_1} \delta_{i_1, i_1} \delta(w_{1'} - w_1), \quad (\text{B7})$$

$$\begin{aligned} \Gamma^\Lambda(1', 2'; 1, 2) &= [\Gamma_{i_1 i_2}^{\Lambda ss}(w_1, w_2; w_1, w_2) \theta_{s_1, s_1}^a \theta_{s_2, s_2}^a \theta_{l_1, l_1}^b \theta_{l_2, l_2}^b \\ &+ \Gamma_{i_1 i_2}^{\Lambda sd}(w_1, w_2; w_1, w_2) \theta_{s_1, s_1}^a \theta_{s_2, s_2}^a \delta_{l_1, l_1} \delta_{l_2, l_2} \\ &+ \Gamma_{i_1 i_2}^{\Lambda ds}(w_1, w_2; w_1, w_2) \delta_{s_1, s_1} \delta_{s_2, s_2} \theta_{l_1, l_1}^b \theta_{l_2, l_2}^b \\ &+ \Gamma_{i_1 i_2}^{\Lambda dd}(w_1, w_2; w_1, w_2) \delta_{s_1, s_1} \delta_{s_2, s_2} \delta_{l_1, l_1} \delta_{l_2, l_2}] \\ &\times \delta_{i_1, i_1} \delta_{i_2, i_2} \delta(w_{1'} + w_{2'} - w_1 - w_2) - (1 \leftrightarrow 2), \end{aligned} \quad (\text{B8})$$

where $a, b \in \{1, 2, 3\}$. The superscripts *ss*, *sd*, *ds*, *dd* hereby denote if the coupling in the spin (valley) sector is spin like (*s*) or density like (*d*).

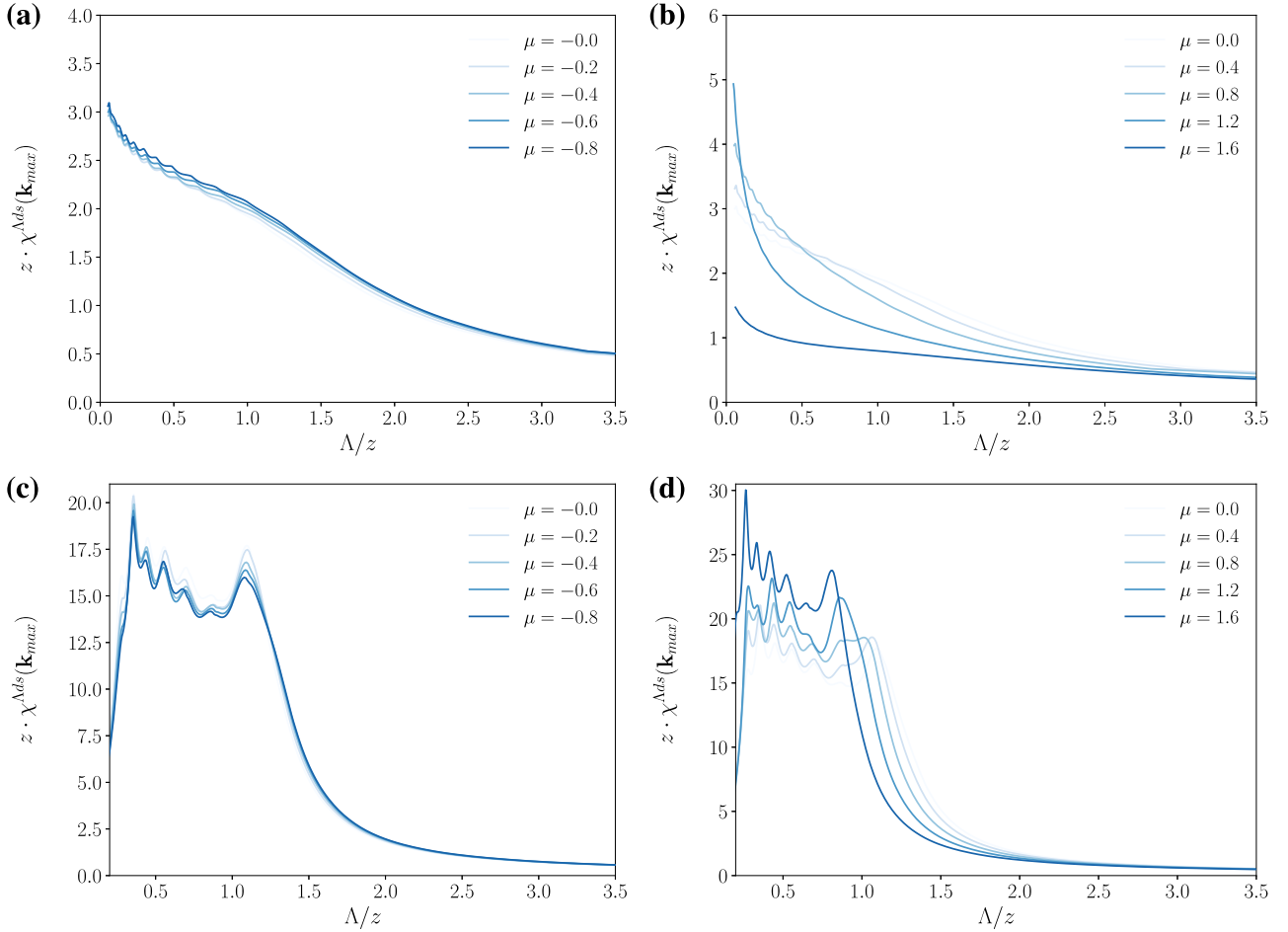


FIG. 7. Effect of level terms on the static structure factor $\chi^{\Lambda ds}(\mathbf{k})$ for the honeycomb lattice. (a), (b) $J_s/J = J_v/J = 1.0$. (c), (d) $J_s/J = 0.5, J_v/J = 4.0$. Similar to what is seen in Fig. 6, unphysical contributions become relevant only at $\mu > 0$, while for negative μ no qualitative change is observed.

The initial conditions at the UV scale then read $\Sigma_{i_1}^\infty(w) = 0$ for the self-energy and

$$\begin{aligned} \Gamma_{i_1 i_2}^{\infty ss}(w_1 w_2'; w_1 w_2) &= J, & \Gamma_{i_1 i_2}^{\infty sd}(w_1 w_2'; w_1 w_2) &= J_s, \\ \Gamma_{i_1 i_2}^{\infty ds}(w_1 w_2'; w_1 w_2) &= J_v, & \Gamma_{i_1 i_2}^{\infty dd}(w_1 w_2'; w_1 w_2) &= 0, \end{aligned} \quad (B9)$$

for the two-particle interaction vertices. Further details on the inner workings of the pf-FRG approach can be found in Ref. [78].

2. Particle-hole symmetry and the half-filling constraint

In the model studied here, the local Hilbert space for fermionic flavors $\alpha \in \{(\uparrow\uparrow), (\uparrow\downarrow), (\downarrow\uparrow), (\downarrow\downarrow)\}$ is equipped with the particle-number basis $B = \{|n_1, \dots, n_4\rangle\}$. We define the linear unitary operator \mathcal{P} acting on the basis by exchanging each occupied state with an empty state $\mathcal{P}|n_1, \dots, n_4\rangle = |1-n_1, \dots, 1-n_4\rangle$. By computing the corresponding matrix elements, one finds that \mathcal{P} transforms creation and annihilation operators into each other, i.e., $\mathcal{P}^\dagger f_\alpha^\dagger \mathcal{P} = f_\alpha$, $\mathcal{P}^\dagger f_\alpha \mathcal{P} = f_\alpha^\dagger$. This transformation leaves the spin-valley Hamiltonian and its

groundstate at $\Lambda \rightarrow \infty$ invariant. On the level of vertex functions, we obtain the identities $\Sigma^\Lambda(1'; 1) = -\Sigma^\Lambda(-1; -1')$ and $\Gamma^\Lambda(1', 2'; 1, 2) = \Gamma^\Lambda(-1, -2; -1', -2')$, where the minus sign applies only to Matsubara frequencies. The vertex components therefore obey $\Sigma_{i_1}^\Lambda(w) = -\Sigma_{i_1}^\Lambda(-w)$ and $\Gamma_{i_1 i_2}^{\Lambda \zeta}(s, t, u) = \Gamma_{i_1 i_2}^{\Lambda \zeta}(-s, t, -u)$ where $\zeta \in \{ss, sd, ds, dd\}$.

These symmetries are explicitly implemented in our pf-FRG approach. However, only one local subspace, namely the one with two occupied states, is mapped to itself by \mathcal{P} , i.e., by enforcing the symmetries of that respective subspace half-filling at each lattice site is expected to be well-enforced on average. Furthermore, since the particle number per site must be conserved as a consequence of local U(1) symmetry, hopping processes that alter the filling would trigger a measurable nonmagnetic instability of the flow, which we do not observe here.

To test the validity of the above considerations we have employed a numerical scheme first exploited in [61]. The spin-valley Hamiltonian is extended by local level terms $\mu \hat{T}_i^\nu \hat{T}_i^\nu$ diagonal in the parton representation of $SU(4)$ spins. Each of them contributes an energy $E(n) = \frac{5}{2}\mu(n - \frac{1}{4}n^2)$ where n is the fermion occupation number. For $\mu < 0$ half-filling (i.e.,

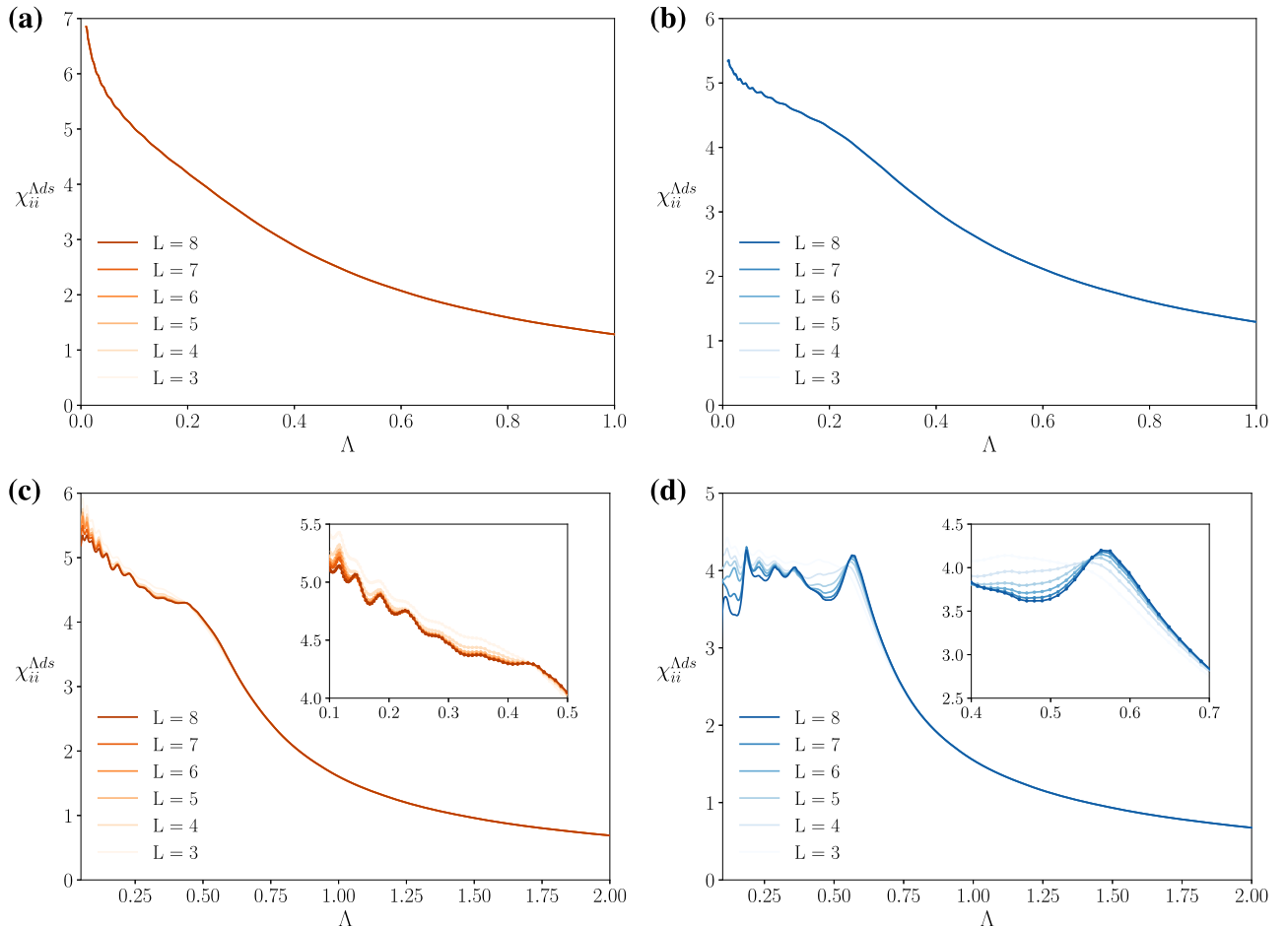


FIG. 8. Finite-size analysis of the onsite correlation function $\chi_{ii}^{\text{AdS}} = \chi_{ii}^{v\Lambda}$ for the triangular lattice (orange) and the honeycomb lattice (blue). (a), (b) $J_s/J = J_v/J = 1.0$. (c), (d) $J_s/J = 0.5, J_v/J = 4.0$. For a paramagnetic ground state the flow shows neither dependence on L nor an instability and correlations quickly decay to zero beyond nearest neighbors.

$n = 2$) is favored, whereas for $\mu > 0$ $E(n)$ is minimized for either $n = 0$ or $n = 4$. Hence, if the assumption of half-filling is correct, then our results at $\mu = 0$ should be consistent with those obtained for negative μ (up to an overall shift of the energy scale). However level attractions ($\mu > 0$) should lead to qualitative changes, since a subspace with different filling is populated.

By repeating our pf-FRG calculations with finite level (repulsion or attraction) terms, such behavior can indeed be observed. While negative values of μ seem to have no qualitative impact, level attraction terms lead to visible changes of the susceptibility flows. In the absence of a breakdown (top row in Figs. 6 and 7) susceptibilities start to vanish, consistent with effective lattice vacancies at $n = 0(4)$. For coupling parameters supporting long-range order (bottom row in Figs. 6 and 7) the effect of positive μ is however less pronounced, numerical instabilities merely shifted towards lower values of Λ . Since the exchange couplings relevant to these phases are usually higher than the simulated ratios μ/J this behavior is expected. In light of these results we are confident that half-filling is well enforced even without an explicit projection scheme.

3. Finite-size analysis of the RG flow

An instability in the vertex function during the RG flow indicates spontaneous breaking of symmetries that have been implemented in the initial conditions [62]. Most prominently, magnetic instabilities appear as pronounced kinks or cusps in the flow of the momentum resolved two-spin correlations. Alternatively, one may check the behavior of an on-site correlation function, i.e., χ_{ii}^Λ , for different values of the vertex range L . Formally, L does not determine the system size (which is in fact infinite in pf-FRG) but rather sets the scale on which spins can be correlated. It is then natural to expect sensitivity to this parameter near the critical scale since the physics is governed by the collective behavior of all spins. However, if the system does not develop an instability down to the smallest energy scales, i.e., the pf-FRG flow stays regular, then real-space correlations should be robust with respect to variations of L .

Indeed as shown in Fig. 8, flows of the spin correlation in the dominant interaction channel for different L are aligned within the paramagnetic regions of the spin-valley phase diagrams, but deviate from each other around the critical scale in the ordered phases. We find, however, that this effect is

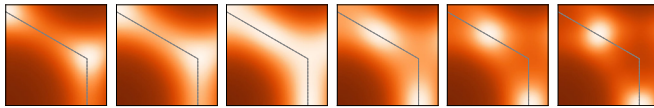


FIG. 9. Structure factors for the SU(4) model on the triangular lattice within the paramagnetic phase. Lines denote the first Brillouin zone boundary. From left to right $J_2/J_1 = 0.0/0.1/0.2/0.3/0.4/0.5$. At a ratio of $J_2/J_1 \approx 0.2$ a deformation from local 120° correlations to local stripe correlations is observed.

more subtle for the triangular than the honeycomb lattice, which we attribute to the inherent geometric frustration of the former.

4. Structure factor evolution in the spin-valley liquid of the J_1 - J_2 model

The spin-valley entangled liquid ground states of the nearest-neighbor SU(4) Heisenberg models (on both the triangular and honeycomb lattice) remain stable upon inclusion of moderate longer-ranged exchange interactions as illustrated in Fig. 3 of the main text.

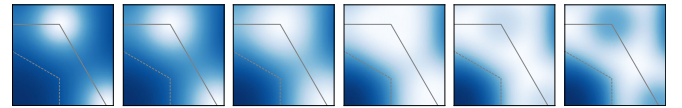


FIG. 10. Structure factors for the SU(4) model on the honeycomb lattice within the paramagnetic phase. Dashed lines denote the first, full lines the extended Brillouin zone. From left to right $J_2/J_1 = 0.0/0.1/0.2/0.3/0.4/0.5$. At a ratio of $J_2/J_1 \approx 0.3$ a deformation from local Néel to local spiral correlations is observed.

Here, we provide further information about the evolution of the structure factors upon varying J_2/J_1 . First, we recall that for $J_2/J_1 = 0$, local correlations are reminiscent of 120° (Néel) order for the triangular (honeycomb) model. Going to large antiferromagnetic $J_2 > 0$, stripe (spiral) order emerges with the evolution of the structure factor being plotted in Figs. 9 and 10 at the onset of these orders. Around $J_2/J_1 \approx 0.2$ for the triangular and at about $J_2/J_1 \approx 0.3$ for the honeycomb lattice, the topology of the momentum resolved correlation functions changes visibly, indicating a Lifshitz transition.

-
- [1] Y. Cao, V. Fatemi, A. Demir, S. Fang, S. L. Tomarken, J. Y. Luo, J. D. Sanchez-Yamagishi, K. Watanabe, T. Taniguchi, E. Kaxiras, *et al.*, Correlated insulator behavior at half-filling in magic-angle graphene superlattices, *Nature* **556**, 80 (2018).
- [2] Y. Cao, V. Fatemi, S. Fang, K. Watanabe, T. Taniguchi, E. Kaxiras, and P. Jarillo-Herrero, Unconventional superconductivity in magic-angle graphene superlattices, *Nature* **556**, 43 (2018).
- [3] M. Yankowitz, S. Chen, H. Polshyn, Y. Zhang, K. Watanabe, T. Taniguchi, D. Graf, A. F. Young, and C. R. Dean, Tuning superconductivity in twisted bilayer graphene, *Science* **363**, 1059 (2019).
- [4] A. L. Sharpe, E. J. Fox, A. W. Barnard, J. Finney, K. Watanabe, T. Taniguchi, M. A. Kastner, and D. Goldhaber-Gordon, Emergent ferromagnetism near three-quarters filling in twisted bilayer graphene, *Science* **365**, 605 (2019).
- [5] X. Lu, P. Stepanov, W. Yang, M. Xie, M. A. Aamir, I. Das, C. Urgell, K. Watanabe, T. Taniguchi, G. Zhang *et al.*, Superconductors, orbital magnets, and correlated states in magic angle bilayer graphene, *Nature* **574**, 653 (2019).
- [6] G. Chen, L. Jiang, S. Wu, B. Lyu, H. Li, B. L. Chittari, K. Watanabe, T. Taniguchi, Z. Shi, J. Jung *et al.*, Evidence of a gate-tunable Mott insulator in a trilayer graphene moiré superlattice, *Nat. Phys.* **15**, 237 (2019).
- [7] G. Chen, A. L. Sharpe, P. Gallagher, I. T. Rosen, E. J. Fox, L. Jiang, B. Lyu, H. Li, K. Watanabe, T. Taniguchi, and *et al.*, Signatures of gate-tunable superconductivity in trilayer graphene/boron nitride moiré superlattice, *Nature* **572**, 215 (2019).
- [8] E. Codecido, Q. Wang, R. Koester, S. Che, H. Tian, R. Lv, S. Tran, K. Watanabe, T. Taniguchi, F. Zhang, *et al.*, Correlated insulating and superconducting states in twisted bilayer graphene below the magic angle, *Sci. Adv.* **5**, eaaw9770 (2019).
- [9] X. Liu, Z. Hao, E. Khalaf, J. Y. Lee, K. Watanabe, T. Taniguchi, A. Vishwanath, and P. Kim, Spin-polarized correlated insulator and superconductor in twisted double bilayer graphene, [arXiv:1903.08130](https://arxiv.org/abs/1903.08130).
- [10] Y. Cao, D. Rodan-Legrain, O. Rubies-Bigordà, J. M. Park, K. Watanabe, T. Taniguchi, and P. Jarillo-Herrero, Electric field tunable correlated states and magnetic phase transitions in twisted bilayer-bilayer graphene, [arXiv:1903.08596](https://arxiv.org/abs/1903.08596).
- [11] C. Shen, N. Li, S. Wang, Y. Zhao, J. Tang, J. Liu, J. Tian, Y. Chu, K. Watanabe, T. Taniguchi *et al.*, Observation of superconductivity with T_c onset at 12K in electrically tunable twisted double bilayer graphene, [arXiv:1903.06952](https://arxiv.org/abs/1903.06952).
- [12] M. Serlin, C. L. Tschorhart, H. Polshyn, Y. Zhang, J. Zhu, K. Watanabe, T. Taniguchi, L. Balents, and A. F. Young, Intrinsic quantized anomalous Hall effect in a moiré heterostructure, *Science* **367**, 900 (2020).
- [13] G. Trambly de Laissardière, D. Mayou, and L. Magaud, Localization of dirac electrons in rotated graphene bilayers, *Nano Lett.* **10**, 804 (2010).
- [14] R. Bistritzer and A. H. MacDonald, Moiré bands in twisted double-layer graphene, *Proc. Natl. Acad. Sci. U.S.A.* **108**, 12233 (2011).
- [15] J. M. B. Lopes dos Santos, N. M. R. Peres, and A. H. Castro Neto, Continuum model of the twisted graphene bilayer, *Phys. Rev. B* **86**, 155449 (2012).
- [16] C. Xu and L. Balents, Topological Superconductivity in Twisted Multilayer Graphene, *Phys. Rev. Lett.* **121**, 087001 (2018).
- [17] N. F. Q. Yuan and L. Fu, Model for the metal-insulator transition in graphene superlattices and beyond, *Phys. Rev. B* **98**, 045103 (2018).
- [18] J. F. Dodaro, S. A. Kivelson, Y. Schattner, X. Q. Sun, and C. Wang, Phases of a phenomenological model of twisted bilayer graphene, *Phys. Rev. B* **98**, 075154 (2018).

- [19] D. M. Kennes, J. Lischner, and C. Karrasch, Strong correlations and $d + id$ superconductivity in twisted bilayer graphene, *Phys. Rev. B* **98**, 241407(R) (2018).
- [20] Q.-K. Tang, L. Yang, D. Wang, F.-C. Zhang, and Q.-H. Wang, Spin-triplet f -wave pairing in twisted bilayer graphene near $\frac{1}{4}$ -filling, *Phys. Rev. B* **99**, 094521 (2019).
- [21] H. Isobe, N. F. Q. Yuan, and L. Fu, Unconventional Superconductivity and Density Waves in Twisted Bilayer Graphene, *Phys. Rev. X* **8**, 041041 (2018).
- [22] Y.-P. Lin and R. M. Nandkishore, Kohn-Luttinger superconductivity on two orbital honeycomb lattice, *Phys. Rev. B* **98**, 214521 (2018).
- [23] Y.-P. Lin and R. M. Nandkishore, A chiral twist on the high- T_c phase diagram in Moiré heterostructures, *Phys. Rev. B* **100**, 085136 (2019).
- [24] L. Rademaker and P. Mellado, Charge-transfer insulation in twisted bilayer graphene, *Phys. Rev. B* **98**, 235158 (2018).
- [25] T. Huang, L. Zhang, and T. Ma, Antiferromagnetically ordered Mott insulator and $d + id$ superconductivity in twisted bilayer graphene: A quantum Monte Carlo study, *Sci. Bull.* **64**, 310 (2019).
- [26] M. Fidrysiak, M. Zegrodnik, and J. Spałek, Unconventional topological superconductivity and phase diagram for an effective two-orbital model as applied to twisted bilayer graphene, *Phys. Rev. B* **98**, 085436 (2018).
- [27] H. Guo, X. Zhu, S. Feng, and R. T. Scalettar, Pairing symmetry of interacting fermions on a twisted bilayer graphene superlattice, *Phys. Rev. B* **97**, 235453 (2018).
- [28] B. Roy and V. Jurićć, Unconventional superconductivity in nearly flat bands in twisted bilayer graphene, *Phys. Rev. B* **99**, 121407(R) (2019).
- [29] C.-C. Liu, L.-D. Zhang, W.-Q. Chen, and F. Yang, Chiral Spin Density Wave and $d + id$ Superconductivity in the Magic-Angle-Twisted Bilayer Graphene, *Phys. Rev. Lett.* **121**, 217001 (2018).
- [30] Y. Da Liao, Z. Y. Meng, and X. Y. Xu, Valence Bond Orders at Charge Neutrality in a Possible Two-Orbital Extended Hubbard Model for Twisted Bilayer Graphene, *Phys. Rev. Lett.* **123**, 157601 (2019).
- [31] Y.-Z. You and A. Vishwanath, Superconductivity from valley fluctuations and approximate SO(4) symmetry in a weak coupling theory of twisted bilayer graphene, *npj Quantum Mater.* **4**, 16 (2019).
- [32] A. Thomson, S. Chatterjee, S. Sachdev, and M. S. Scheurer, Triangular antiferromagnetism on the honeycomb lattice of twisted bilayer graphene, *Phys. Rev. B* **98**, 075109 (2018).
- [33] Y. Sherkunov and J. J. Betouras, Electronic phases in twisted bilayer graphene at magic angles as a result of Van Hove singularities and interactions, *Phys. Rev. B* **98**, 205151 (2018).
- [34] J. Kang and O. Vafek, Strong Coupling Phases of Partially Filled Twisted Bilayer Graphene Narrow Bands, *Phys. Rev. Lett.* **122**, 246401 (2019).
- [35] Y.-H. Zhang, D. Mao, Y. Cao, P. Jarillo-Herrero, and T. Senthil, Nearly flat chern bands in moiré superlattices, *Phys. Rev. B* **99**, 075127 (2019).
- [36] C. Schrade and L. Fu, Spin-valley density wave in moiré materials, *Phys. Rev. B* **100**, 035413 (2019).
- [37] K. Seo, V. N. Kotov, and B. Uchoa, Ferromagnetic Mott State in Twisted Graphene Bilayers at the Magic Angle, *Phys. Rev. Lett.* **122**, 246402 (2019).
- [38] M. Koshino, N. F. Q. Yuan, T. Koretsune, M. Ochi, K. Kuroki, and L. Fu, Maximally Localized Wannier Orbitals and the Extended Hubbard Model for Twisted Bilayer Graphene, *Phys. Rev. X* **8**, 031087 (2018).
- [39] J. Kang and O. Vafek, Symmetry, Maximally Localized Wannier States, and a Low-Energy Model for Twisted Bilayer Graphene Narrow Bands, *Phys. Rev. X* **8**, 031088 (2018).
- [40] L. Classen, C. Honerkamp, and M. M. Scherer, Competing phases of interacting electrons on triangular lattices in moiré heterostructures, *Phys. Rev. B* **99**, 195120 (2019).
- [41] H. C. Po, L. Zou, A. Vishwanath, and T. Senthil, Origin of Mott Insulating Behavior and Superconductivity in Twisted Bilayer Graphene, *Phys. Rev. X* **8**, 031089 (2018).
- [42] L. Xian, D. M. Kennes, N. Tancogne-Dejean, M. Altarelli, and A. Rubio, Multiflat bands and strong correlations in twisted bilayer boron nitride: Doping-induced correlated insulator and superconductor, *Nano Lett.* **19**, 4934 (2019).
- [43] Y.-H. Zhang and T. Senthil, Bridging hubbard model physics and quantum Hall physics in trilayer graphene/h – BN moiré superlattice, *Phys. Rev. B* **99**, 205150 (2019).
- [44] T. M. R. Wolf, J. L. Lado, G. Blatter, and O. Zilberberg, Electrically Tunable Flat Bands and Magnetism in Twisted Bilayer Graphene, *Phys. Rev. Lett.* **123**, 096802 (2019).
- [45] J. C. W. Song, P. Samutpraphoot, and L. S. Levitov, Topological Bloch bands in graphene superlattices, *Proc. Natl. Acad. Sci. USA* **112**, 10879 (2015).
- [46] Q. Tong, H. Yu, Q. Zhu, Y. Wang, X. Xu, and W. Yao, Topological mosaics in moiré superlattices of van der Waals heterobilayers, *Nat. Phys.* **13**, 356 (2017).
- [47] T. M. R. Wolf, O. Zilberberg, I. Levkivskyi, and G. Blatter, Substrate-induced topological minibands in graphene, *Phys. Rev. B* **98**, 125408 (2018).
- [48] B. L. Chittari, G. Chen, Y. Zhang, F. Wang, and J. Jung, Gate-Tunable Topological Flat Bands in Trilayer Graphene Boron-Nitride Moiré Superlattices, *Phys. Rev. Lett.* **122**, 016401 (2019).
- [49] L. Zou, H. C. Po, A. Vishwanath, and T. Senthil, Band structure of twisted bilayer graphene: Emergent symmetries, commensurate approximants, and Wannier obstructions, *Phys. Rev. B* **98**, 085435 (2018).
- [50] H. C. Po, L. Zou, T. Senthil, and A. Vishwanath, Faithful tight-binding models and fragile topology of magic-angle bilayer graphene, *Phys. Rev. B* **99**, 195455 (2019).
- [51] S. Carr, S. Fang, H. C. Po, A. Vishwanath, and E. Kaxiras, Derivation of Wannier orbitals and minimal-basis tight-binding Hamiltonians for twisted bilayer graphene: First-principles approach, *Phys. Rev. Res.* **1**, 033072 (2019).
- [52] G. Khaliullin, Orbital order and fluctuations in Mott insulators, *Prog. Theor. Phys. Suppl.* **160**, 155 (2005).
- [53] P. Corboz, M. Lajkó, A. M. Läuchli, K. Penc, and F. Mila, Spin-Orbital Quantum Liquid on the Honeycomb Lattice, *Phys. Rev. X* **2**, 041013 (2012).
- [54] W. M. H. Natori, R. Nutakki, R. G. Pereira, and E. C. Andrade, SU(4) Heisenberg model on the honeycomb lattice with exchange-frustrated perturbations: Implications for twistronics and Mott insulators, *Phys. Rev. B* **100**, 205131 (2019).
- [55] X.-C. Wu, A. Keselman, C.-M. Jian, K. A. Pawlak, and C. Xu, Ferromagnetism and spin-valley liquid states in moiré correlated insulators, *Phys. Rev. B* **100**, 024421 (2019).

- [56] D. P. Arovas and A. Auerbach, Functional integral theories of low-dimensional quantum Heisenberg models, *Phys. Rev. B* **38**, 316 (1988).
- [57] J. Reuther and P. Wölfle, J_1 - J_2 frustrated two-dimensional Heisenberg model: Random phase approximation and functional renormalization group, *Phys. Rev. B* **81**, 144410 (2010).
- [58] J. Reuther and R. Thomale, Functional renormalization group for the anisotropic triangular antiferromagnet, *Phys. Rev. B* **83**, 024402 (2011).
- [59] J. Reuther, D. A. Abanin, and R. Thomale, Magnetic order and paramagnetic phases in the quantum J_1 - J_2 - J_3 honeycomb model, *Phys. Rev. B* **84**, 014417 (2011).
- [60] C. Wetterich, Exact evolution equation for the effective potential, *Phys. Lett. B* **301**, 90 (1993).
- [61] M. L. Baez and J. Reuther, Numerical treatment of spin systems with unrestricted spin length S : A functional renormalization group study, *Phys. Rev. B* **96**, 045144 (2017).
- [62] F. L. Buessen, D. Roscher, S. Diehl, and S. Trebst, Functional renormalization group approach to $SU(N)$ Heisenberg models: Real-space renormalization group at arbitrary N , *Phys. Rev. B* **97**, 064415 (2018).
- [63] D. Roscher, F. L. Buessen, M. M. Scherer, S. Trebst, and S. Diehl, Functional renormalization group approach to $SU(N)$ Heisenberg models: Momentum-space renormalization group for the large- N limit, *Phys. Rev. B* **97**, 064416 (2018).
- [64] D. Roscher, N. Gneist, M. M. Scherer, S. Trebst, and S. Diehl, Cluster functional renormalization group and absence of a bilinear spin liquid in the J_1 - J_2 -Heisenberg model, *Phys. Rev. B* **100**, 125130 (2019).
- [65] Generally, an instability can be observed for any (quantum) order which is captured by a fermionic bilinear operator; see Ref. [62]. More complicated order whose order parameter involves higher order operators does not necessarily manifest in a flow breakdown.
- [66] J. B. Marston and I. Affleck, Large- n limit of the Hubbard-Heisenberg model, *Phys. Rev. B* **39**, 11538 (1989).
- [67] D. S. Rokhsar, Quadratic quantum antiferromagnets in the fermionic large- N limit, *Phys. Rev. B* **42**, 2526 (1990).
- [68] E. Lieb, T. Schultz, and D. Mattis, Two soluble models of an antiferromagnetic chain, *Ann. Phys.* **16**, 407 (1961).
- [69] M. B. Hastings, Lieb-Schultz-Mattis in higher dimensions, *Phys. Rev. B* **69**, 104431 (2004).
- [70] Y. Yao, C.-T. Hsieh, and M. Oshikawa, Anomaly Matching and Symmetry-Preserved Critical Phases in $SU(N)$ Spin Systems in 1+1 Dimensions, *Phys. Rev. Lett.* **123**, 180201 (2019).
- [71] We finally note that, in principle, the FRG setup can also be extended to allow for a continuation of the flow into the ordered regime [63,64,79]; however, such modifications are beyond the scope of this work.
- [72] Z. Zhu and S. R. White, Spin liquid phase of the $S = \frac{1}{2}J_1 - J_2$ Heisenberg model on the triangular lattice, *Phys. Rev. B* **92**, 041105(R) (2015).
- [73] W.-J. Hu, S.-S. Gong, W. Zhu, and D. N. Sheng, Competing spin-liquid states in the spin- $\frac{1}{2}$ Heisenberg model on the triangular lattice, *Phys. Rev. B* **92**, 140403(R) (2015).
- [74] Y. Iqbal, W.-J. Hu, R. Thomale, D. Poilblanc, and F. Becca, Spin liquid nature in the heisenberg $J_1 - J_2$ triangular antiferromagnet, *Phys. Rev. B* **93**, 144411 (2016).
- [75] Y.-H. Zhang and D. Mao, Spin liquids and pseudogap metals in $SU(4)$ Hubbard model in moiré superlattice, *Phys. Rev. B* **101**, 035122 (2020).
- [76] Y. Iqbal, R. Thomale, F. Parisen Toldin, S. Rachel, and J. Reuther, Functional renormalization group for three-dimensional quantum magnetism, *Phys. Rev. B* **94**, 140408(R) (2016).
- [77] J. Reuther and R. Thomale, Cluster functional renormalization group, *Phys. Rev. B* **89**, 024412 (2014).
- [78] F. L. Buessen, A functional renormalization group perspective on quantum spin liquids in three-dimensional frustrated magnets, Ph.D. thesis, University of Cologne, 2019.
- [79] M. Salmhofer, C. Honerkamp, W. Metzner, and O. Lauscher, Renormalization group flows into phases with broken symmetry, *Prog. Theor. Phys.* **112**, 943 (2004).